Photonic Synthesis and Coating of High-Entropy Oxide on Layered Ni-Rich Cathode Particles

Yanyan Cui, Yushu Tang, Jing Lin, Junbo Wang, Horst Hahn, Ben Breitung, Simon Schweidler,* Torsten Brezesinski,* and Miriam Botros*

High-entropy materials have drawn much attention as battery materials due to their distinctive properties. Lithiated high-entropy oxide ($Li_{0.33}$ $(MgCoNiCuZn)_{0.67}O$, LiHEO) exhibits both high lithium-ion and electronic conductivity, making it a potential coating material for layered Ni-rich oxide cathodes ($Li_{1+x}(Ni_{1-y-z}Co_yMn_z)_{1-x}O_2$, NCM or NMC) in conventional Li-ion battery cells; however, high-temperature synthesis limits its application. Therefore, a photonic curing strategy is used for synthesizing LiHEO and the non-lithiated form (denoted as high-entropy oxide [HEO]), and nanoscale coatings are successfully produced on $LiNi_{0.85}Co_{0.1}Mn_{0.05}O_2$ (NCM851005) particles. To one's knowledge, this is the first report on particle coating with high-entropy materials using photonic curing. NCM851005 with LiHEO-modified surface shows good cycling stability, with a capacity retention of 97% at 1 C rate after 200 cycles. The improvement in electrochemical performance is attributed to the conformal coating that prevents structural changes caused by the reaction between cathode material and liquid electrolyte. Compared to bare NCM851005, the coated material shows a significantly reduced tendency for intergranular cracking, successfully preventing electrolyte penetration and suppressing side reactions. Overall, photonic curing presents a novel cost- and energy-efficient synthesis and coating procedure that paves the way for surface modification of any heat-sensitive material for a wide range of applications.

1. Introduction

With the increasing utilization of Li-ion batteries (LIBs) in portable electronics, medical devices, and electric vehicles, there is a growing demand for electrochemical energy storage with higher power and energy density.[1–3] Cathode materials, playing a dominating role in the LIB performance, have been studied to enhance the energy density and meet the requirements of high-performance batteries. Among the existing cathode materials, layered lithium transition metal (TM) oxides ($Li_{1+x}(Ni_{1-y-z}Co_yMn_z)_{1-x}O_2$, NCM or NMC), with a Ni content exceeding 80%, are considered promising candidates for advanced LIBs due to their lower cost resulting from a low Co content and high specific capacity based on Ni redox.[4–7] However, Ni-rich NCMs suffer from poor cycle life and capacity fading due to the highly reactive Ni^{4+} species formed upon charging. The latter can interact with the electrolyte and promote surface degradation, eventually resulting in structural transformation from layered to rock-salt structure (accompanied by oxygen loss), among others.[8,9]

Numerous studies have investigated Ni-rich NCM cathodes, and surface coating has been demonstrated as an effective strategy to suppress interfacial side reactions to different degrees, including electrolyte decomposition and TM dissolution.[10,11] Various coating materials have been proposed for improving the electrochemical performance of NCMs. Based on their properties, two types of coatings are discussed here, namely redox-inactive materials and those exhibiting reasonably high ionic and electronic partial conductivities. The inactive coating materials, such as Al_2O_3,[12,13] ZrO_2,[14] or Li_3PO_4,[15,16] act as a physical (protective) barrier, thereby reducing side reactions between cathode material and electrolyte. The ionically and/or electronically conductive

Y. Cui, Y. Tang, J. Lin, J. Wang, H. Hahn, B. Breitung, S. Schweidler, T. Brezesinski, M. Botros
Institute of Nanotechnology
Karlsruhe Institute of Technology (KIT)
Kaiserstr. 12, 76131 Karlsruhe, Germany
E-mail: simon.schweidler@kit.edu; torsten.brezesinski@kit.edu; miriam.botros@kit.edu

The ORCID identification number(s) for the author(s) of this article can be found under https://doi.org/10.1002/sstr.202400197.

H. Hahn
KIT-TUD Joint Research Laboratory Nanomaterials
Institute of Materials Science
Technische Universität Darmstadt
Alarich-Weiss-Str. 2, 64287 Darmstadt, Germany

H. Hahn
School of Sustainable Chemical, Biological and Materials Engineering
University of Oklahoma
Norman, OK 73019, USA

coating materials include, e.g., lithiated metal oxides, solid electrolytes, carbon, and polymers. Mixed ionic–electronic conductors as coating materials not only exhibit good electrochemical stability, similar to inactive coating materials, but also help to boost charge transfer at the cathode side, leading to improved rate performance.

Common methods of coating NCMs are wet-chemical or chemical vapor deposition techniques, such as atomic layer deposition (ALD).[10] However, wet-chemical coating processes often suffer from nonuniformities, while the homogeneous and conformal coating by ALD is cost inefficient and faces considerable challenges for industrial application, especially with regards to compositionally complex materials.[17] Therefore, it is necessary to find coating materials with tailored electrical properties that are attainable by a scalable technology.

High-entropy oxides (HEOs) have recently drawn attention due to their unique attributes. Bérardan et al. reported that Li-doped rock-salt-type HEOs ($Li_x(MgCoNiCuZn)_{1-x}O$) may exhibit high ionic conductivity at room temperature, rendering them suitable for application as lithium-ion conductors.[18] They observed that the conductivity of HEOs is enhanced with increasing lithium content, reaching a maximum at around 30 mol% ($\approx 10^{-3}$ S cm^{-1}), which is five orders of magnitude higher than that of the undoped counterpart ($\approx 10^{-8}$ S cm^{-1}). This enhancement may be attributed to the substitution of cations in HEOs by lithium ions via an intrinsic charge compensation mechanism. This results in a combination of +1 and +3 elements or in the creation of oxygen vacancies while maintaining the rock-salt structure, opening possible diffusion pathways for lithium through the lattice and thus increasing conductivity. Later, Moździerz et al. found that the contribution of the electronic partial conductivity increases significantly with higher lithium doping, alongside the ionic conductivity.[19] Therefore, Li-doped HEOs (LiHEOs) should be classified as mixed ionic–electronic conductors rather than potential candidates for solid electrolytes. Overall, LiHEO could be an interesting material for coating of active electrode particles in LIBs owing to its relatively high electronic and ionic conductivity.

Generally, the synthesis of rock-salt-type HEOs is performed at high temperatures or requires very long mechanical milling times. However, high temperatures or extended ball milling can cause structural damage to the NCM, making the conventional method of synthesizing HEOs unsuitable for coating. Therefore, photonic curing is introduced, which, to our knowledge, is used for the first time to rapidly produce HEOs with a single-phase rock-salt structure at low environmental temperatures. In the present work, NCM851005 was coated with both HEO and LiHEO using the photonic curing technique to produce a uniform layer on the surface of the cathode particles. This approach effectively prevents reactions between the cathode material and the electrolyte, significantly improving the structural stability of the active material particles and therefore the cycling performance. In addition, by comparing LiHEO- and HEO-coated NCM851005, it was found that the increase in conductivity upon lithium doping plays a crucial role in enhancing performance.

This novel coating technology, combined with the compositional versatility of the coating materials, opens up new possibilities beyond LIB applications. These include solid-state batteries, electrocatalysis, or energy conversion, allowing a broader scope for functional coatings.

2. Results and Discussion

The LiHEO and HEO coatings were prepared as described in Experimental Section using a wet-chemical method by means of photonic curing, followed by annealing. In this process, NCM851005 particles were suspended in nitrate-based precursor solutions of LiHEO or HEO. After the solvent (ethanol) was evaporated, photonic curing was employed to produce and synthesize the coating. The LiHEO- and HEO-coated NCM851005 samples were heated at 600 °C for 2 h in air to remove lithium residuals from the coating process, e.g., LiOH, and under oxygen to additionally reduce the amount of carbonates on the particle surface. Note that the annealing step might also increase the uniformity of the surface coating. Finally, the powders were stored in an Ar-filled glove box. A schematic of the photonic curing process is depicted in **Figure 1**.

In the following, the NCM851005 particles coated with HEO and LiHEO are referred to as HEO@NCM851005 and LiHEO@NCM851005, respectively. Raman spectroscopy was performed to detect possible impurities. The measurements revealed the presence of carbonate impurities (1075 cm^{-1}) on the surface of the coated samples (Figure S1, Supporting Information), which could be one of the reasons for the poor performance of the NCM851005 directly after photonic curing. To address this issue and mitigate the impact of surface impurities, the materials were annealed in oxygen and air, respectively. Additionally, the posttreatment is expected to enhance contact and uniformity of the coating, as well as possibly promoting elemental interdiffusion. The Raman data indicate reduction of surface residuals after annealing.

The following discussions focus on the material properties of the bare (uncoated) and coated NCMs after heating, as well as on the mechanism that is possibly responsible for the enhanced stability. X-ray diffraction (XRD) patterns of the bare NCM851005, HEO@NCM851005, and LiHEO@NCM851005 are compared in Figure S2, Supporting Information. All reflections can be indexed based on a hexagonal structure with $R\bar{3}m$
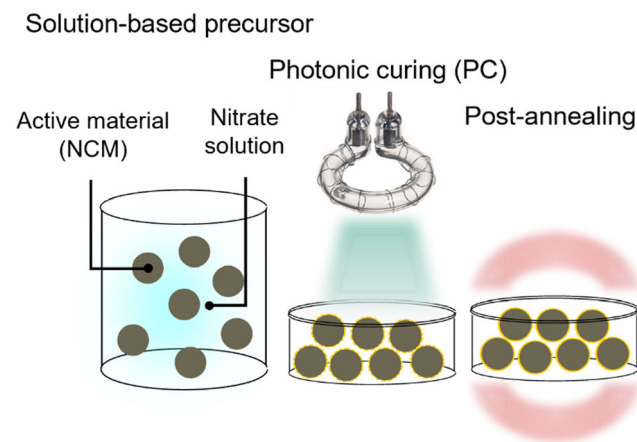

Figure 1. Schematic illustration of LiHEO/HEO coating on NCM particles.

ADVANCED
SCIENCE NEWS
www.advancedsciencenews.com

small
structures
www.small-structures.com

space group, without apparent differences among the materials. No shifts are evident in the patterns of the coated samples, indicating the absence of lattice expansion or contraction in the presence of HEO or LiHEO. The splitting of the (006)/(102) and (108)/(110) reflections for all samples demonstrates that they have a well-developed layered structure. This suggests that neither the coating process nor the posttreatment (including different atmospheres) affects the crystal structure of NCM851005. However, it is notable that the reflections corresponding to the rock-salt structure of HEO and LiHEO are absent, which is due to the low overall coating content (thickness).

Figure 2a–e presents scanning electron microscopy (SEM) images of the materials after annealing in air. It can be observed that the particle shape before and after surface modification remains similar, indicating that the coating process has a negligible effect on the morphology of NCM851005. The high-magnification images show that the top surface of the bare NCM851005 sary particles is rather clean and smooth, while LiHEO@NCM851005 exhibits a rough morphology, with nanometer-sized particles residing on the surface. Energy-dispersive X-ray (EDX) spectroscopy mapping (Figure 2e) was performed to examine the distribution of coating elements on the surface of NCM851005. The mapping of Ni, Co, Mn, O, Mg, Cu,

and Zn indicates that these elements are indeed uniformly distributed in the selected area. SEM–EDX does not provide information on the depth distribution of the respective elements, due to the large probing depth in the micrometer range. However, Mg does exhibit a stronger signal, which might indicate its presence closer to the particle surface when compared to the other elements.

To further confirm the formation, structure, and homogeneity of the HEO and LiHEO coatings, scanning transmission electron microscopy (STEM) measurements in high-angle annular dark-field (HAADF) mode were conducted on the samples (Figure 3a–f and S3, Supporting Information) after annealing in air. As evident from the data, a conformal coating of thickness between 10 and 20 nm was deposited onto the NCM851005 sary particles. The STEM–EDX mapping results confirm the higher Co content in the surface layer compared to the NCM851005. The mapping also indicates that Co is uniformly distributed in the coating. The same applies to Mg, in good agreement with the SEM–EDX data (on a larger scale). As the Ni content in the coating is lower compared to the NCM851005 particles, it is difficult to determine from the mapping whether Ni is evenly distributed on the particle surface. However, it seems that it is also uniformly distributed. However, Cu and Zn did not show
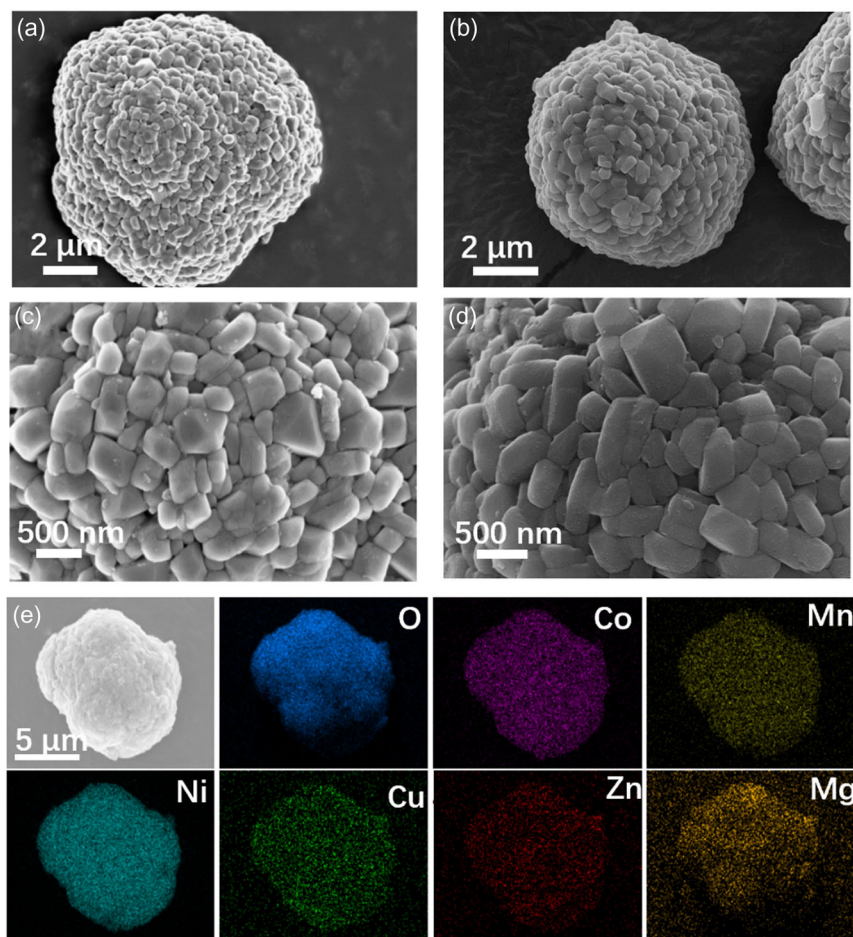

Figure 2. a) SEM image of bare NCM851005; b) LiHEO@NCM851005; and c,d) corresponding magnified images. e) SEM–EDX mapping of LiHEO-coated NCM851005.
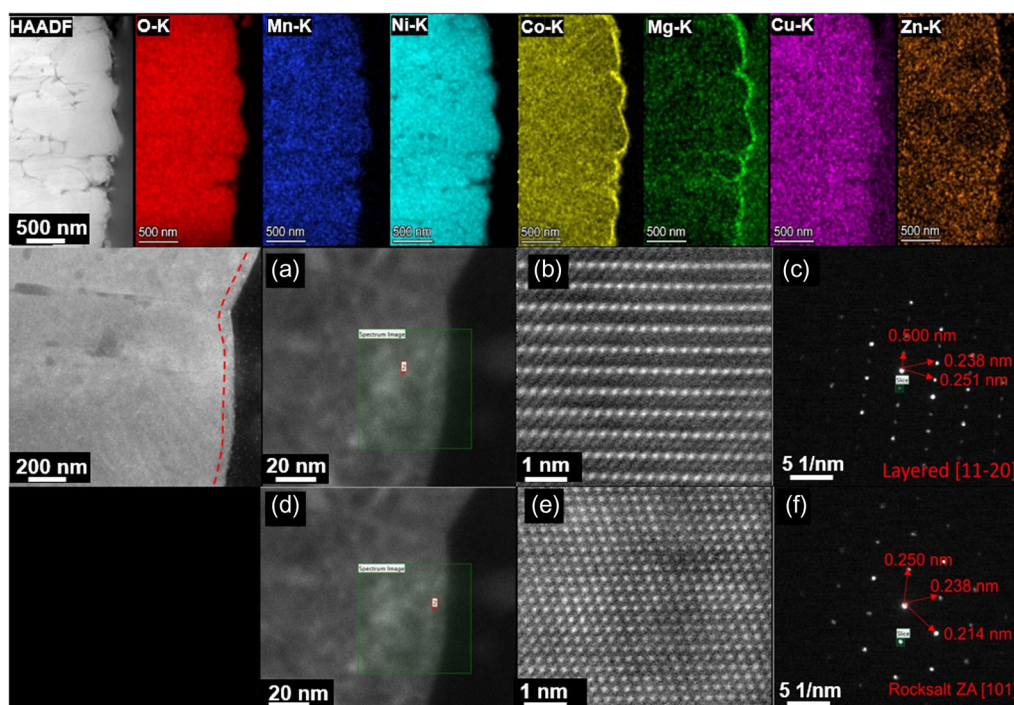
Figure 3. (Top) STEM–HAADF imaging of LiHEO@NCM851005 with EDX mapping results. a–e) Higher-magnification images and c,f) corresponding CBED patterns of the areas marked by the red spots in the green boxes, indicating layered (bulk) and rock-salt (surface) structures.

significant segregation in the coating, which may be due to diffusion into the interior of the NCM851005 particles during the preparation process. Elemental interdiffusion might contribute to the improvement in cycling performance of the NCM851005.[20] While the photonic curing conditions were optimized to achieve single-phase rock-salt structures of the respective materials (Figure S4, Supporting Information), with all elements incorporated on the cationic lattice site, thus forming an HEO with a configurational entropy of 1.61 R, determination of the elemental composition of the coatings on the NCM851005 particles is rather difficult and some variation in the configurational entropy is expected due to elemental interdiffusion.

Figure 3a–f further shows higher-magnification images and corresponding convergent beam electron diffraction (CBED) patterns of the bulk and surface of LiHEO@NCM851005. The lattice spacings of 0.238, 0.251, and 0.500 nm correspond to the (220), (104), and (003) crystal planes of NCM851005, respectively (Figure 3c), which is consistent with the XRD results. In contrast, the surface exhibits a rock-salt structure (Figure 3f), with lattice spacings of 0.214, 0.238, and 0.250 nm, corresponding to the (003), (012), and (220) crystal planes, respectively. These results confirm the formation of the rock-salt-type LiHEO, which is uniformly coated on the surface of the NCM851005 sary particles.

To reveal the influence of the LiHEO and HEO coatings on cycling performance, a series of electrochemical tests were performed. **Figure 4**a–d shows the electrochemical characteristics of NCM851005 coated with HEO and LiHEO after annealing. Both samples, without posttreatment, exhibited lower specific capacities than the bare NCM851005 and higher overpotentials during

cycling (Figure S5, Supporting Information). Therefore, an annealing step was added to sinter the coating and improve its uniformity and conformity. The posttreatment may also facilitate cation interdiffusion and decomposition/consumption of lithium residuals present on the particle surface.

The performance of the samples subjected to posttreatment in air was evaluated at C rates ranging from 0.1 C to 1 °C, with $1\,C = 200\,mA\,g^{-1}$, in the potential range between 2.8 and 4.3 V vs. Li^+/Li. In the rate capability test (Figure 4a and S6a, Supporting Information), the capacities achieved with the LiHEO@NCM851005 at 0.5, 1, 2, 3, and 5 C were comparable to those of the uncoated NCM851005. However, the capacity was lower for a rate of 1 °C, which may be due to the lower ionic conductivity of the coating compared to bulk NCM851005. It is noteworthy that the LiHEO-coated material delivered a higher capacity at 0.5 C than the uncoated counterpart after multiple cycles at the different C rates. This indicates that the coating has a positive effect on the capacity retention after exposure to high C rates. The HEO@NCM851005 (Figure S6, Supporting Information) delivered lower capacities compared to the bare and LiHEO-coated NCM851005 in the rate capability test. This discrepancy can be attributed to the low electronic and ionic partial conductivities of HEO, which deteriorates the electrochemical performance. The capacity retention of LiHEO@NCM851005 after 200 cycles at 1 C was 97.6%, compared to 97.5% and 87.9% for HEO-coated and bare NCM851005, respectively (Figure 4b and S6b, Supporting Information). Although the capacity of the cells using the coated materials was lower in the first 20 cycles, it was significantly higher compared to bare NCM851005 in the following cycles. This is probably because
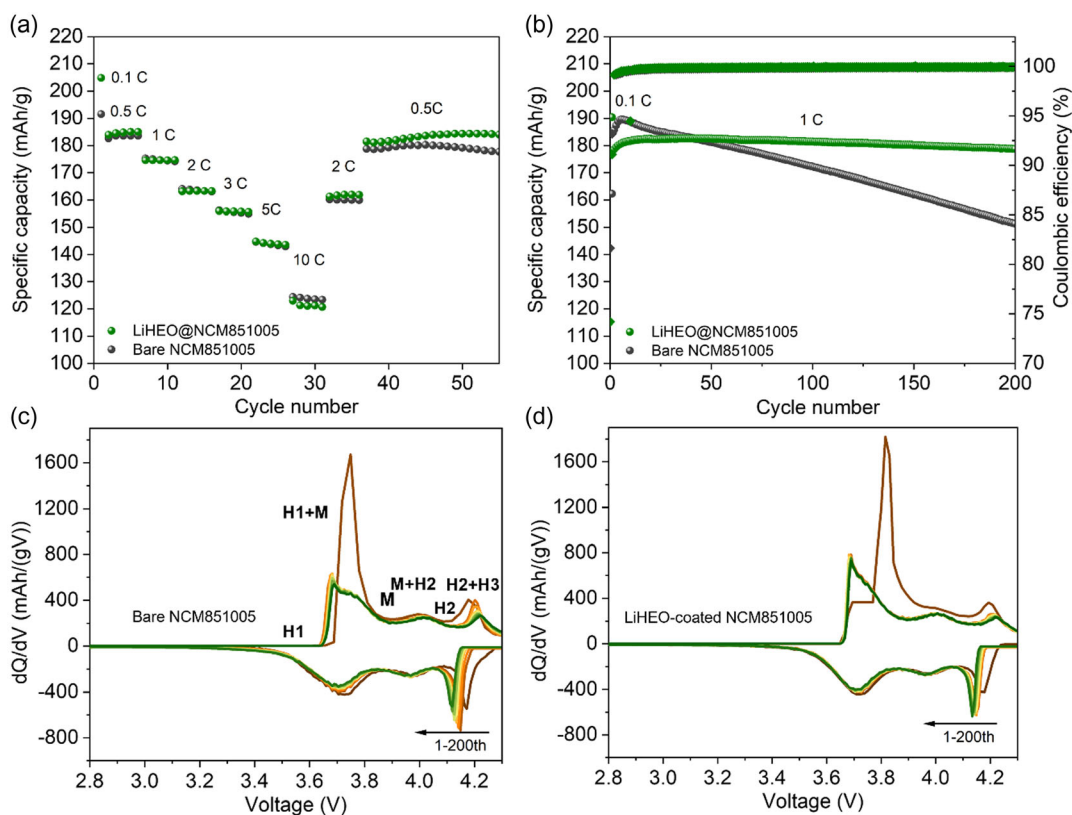
Figure 4. Galvanostatic cycling of bare NCM851005 and LiHEO@NCM851005 in the potential window of 2.8–4.3 V vs. Li$^+$/Li. a) Rate capability testing and b) long-term cycling performance at 1 C. c,d) Corresponding dQ/dV curves (1st to 200th cycle).

the coatings themselves do not provide lithium-ion storage capacity in the applied potential range and may initially hinder ion transport to some extent, due to moderate ionic conductivity and nonideal coating thickness (should ideally be <5 nm), thus impeding the full utilization of the lithium inventory of NCM851005 during cycling.[13] The electronic contribution of the coating also needs to be considered, especially for "thicker" coatings, possibly impeding electron transfer and also resulting in lower capacities. We note that the capacities at 1 C upon long-term cycling are slightly higher than those achieved during the rate capability test. This is expected, since the cycling history of the cells is different. Additionally, this effect is more evident for the bare NCM851005, reaching higher capacities than the coated counterpart during the first 25 cycles, however quickly fading to lower values. This can be attributed to irreversible capacity arising from the uncontrolled formation of cathode–electrolyte interphase, a process less pronounced during the rate test due to better conditioning of the cell at lower C rates before reaching 1 C. To exclude any effect of air calcination on the NCM851005, the bare material was also treated under the same conditions, followed by electrochemical testing. The data collected demonstrate that the cycling stability is better than that of the reference NCM851005 (before heating), but it is also inferior to that of the coated samples. According to reports available in the literature,[21] the posttreated material should still contain lithium residuals on the surface, which exert some effect on the cyclability. By contrast, oxygen treatment leads to much faster capacity

decay. This result indicates a synergetic effect between the coating and the lithium-containing residuals, e.g., carbonate species, which—with an optimal amount—positively affect cycling performance by preventing interfacial reactions with the electrolyte.[22,23]

To examine the electrochemical behavior with the phase transitions occurring upon cycling, differential capacity plots are shown in Figure 4c,d. In general, NCM851005 undergoes a series of phase transitions during the insertion/extraction of Li ions into/from the material, from hexagonal H1 via monoclinic M to hexagonal H2 and hexagonal H3.[24] The high-potential phase transition (H2–H3 region) of NCM851005 is similar to that of LiNiO$_2$ and is accompanied by an abrupt c lattice parameter contraction, leading to secondary particle fracture (intergranular cracking) and associated capacity decay due to the occurrence of side reactions (electrolyte decomposition on new surfaces). Due to degradation during cycling, the position of the oxidation (anodic) and reduction (cathodic) peaks in the dQ/dV plots shifts to higher and lower potentials, respectively, and the peak areas decrease. This indicates that cell polarization becomes more pronounced (impedance growth) as the number of cycles increases. The changes in H2–H3 phase transition with cycling point toward structural stability issues of NCM851005, especially in the uncoated form, which helps explain the differences seen in the capacity fading among the samples. Voltage hysteresis is suppressed more effectively in case of the LiHEO@NCM851005; the dQ/dV curves barely change after

the initial cycles, meaning the H2–H3 phase transition is well maintained.

The microstructural degradation of the NCM851005 sary particles upon cycling was investigated by focused-Ga-ion beam (FIB)–SEM and STEM–HAADF imaging. The bare and coated materials exhibit significantly different microstructural characteristics after 200 cycles at 1 C rate, as shown in **Figure 5**a–d. An SEM image of the pristine sample, prior to cycling, is presented in Figure 5a. As evident, the secondary particle consists of smaller primary particles and is surrounded by polymer binder and carbon black. After cycling, a high density of intergranular cracks is found around the primary particles of the
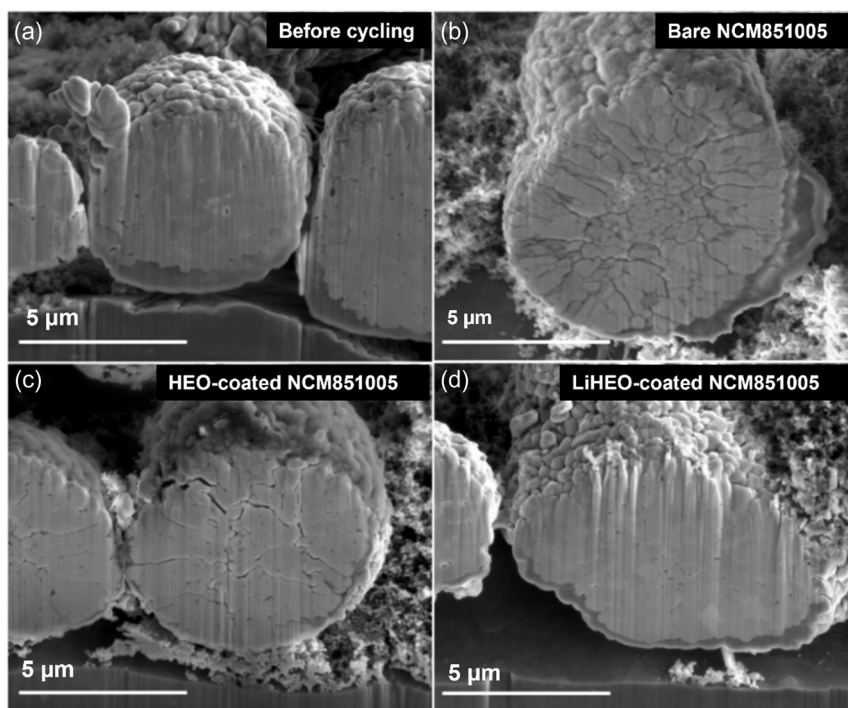

Figure 5. FIB–SEM of bare NCM851005 and HEO- and LiHEO-coated NCM851005 sary particle cross sections. a) Before cycling and b–d) after 200 cycles at 1 C rate.
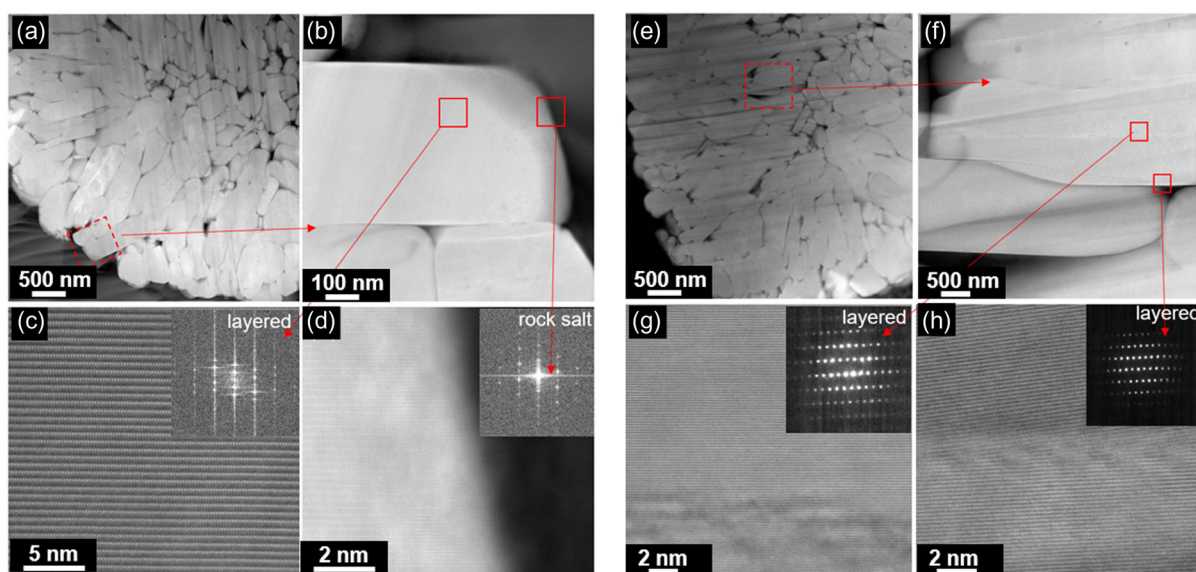

Figure 6. a–d) Surface and e–h) bulk structural degradation of LiHEO@NCM851005 after 200 cycles at 1 C analyzed by STEM–HAADF imaging at different magnifications.

**ADVANCED
SCIENCE NEWS**

www.advancedsciencenews.com

**small
structures**

www.small-structures.com

uncoated NCM851005 (Figure 5b), which is usually considered being one of the major degradation mechanisms leading to cathode failure during extended cycling. Microcrack formation/particle fracture leads to penetration of electrolyte into the particle interior along the grain boundaries and triggers unwanted side reactions, accelerating structural degradation and consumption of lithium inventory. In contrast, reduced cracking is observed for HEO@NCM851005 (Figure 5c), while the LiHEO-coated material was apparently capable of completely suppressing intergranular crack formation during battery operation (Figure 5d). The suppression of particle fracture can be attributed to several mechanisms: the coating provides a physical barrier between the cathode material and the liquid electrolyte, thereby minimizing the contact area and side reactions leading to structural degradation at the interface. This prevents electrolyte penetration into the secondary particle, causing further damage along the grain boundaries between primary particles. Moreover, elemental diffusion from the coating into the NCM851005 primary particles might alter the volume expansion/contraction behavior during cycling; however, more evidence is necessary for a detailed analysis of the stabilization mechanism(s) of the HEO and LiHEO coatings.

To reveal the effect of coatings on the NCM851005 surface and bulk structure (on the atomic level), the materials after cycling were probed using STEM in HAADF mode (**Figure 6**a–h and S7 and S8, Supporting Information). A rock-salt-like phase was observed on the outer surface of the secondary particles for all coated and uncoated samples, as depicted in fast Fourier transform and CBED patterns in the inset of the higher magnification images. In case of the LiHEO@NCM851005, the transition is from layered to rock salt, with the thickness of the latter phase being about 5 nm. However, no phase transition occurred at the internal grain boundaries. This may be due to the fact that the coating prevents electrolyte from penetrating into the bulk, thereby limiting side reactions at the secondary particle–electrolyte interface. In contrast, bare NCM851005 undergoes more severe structural changes at the surface and in the bulk (Figure S7, Supporting Information), with the surface experiencing a phase change up to a depth of $\approx$90 nm. HEO@NCM851005 revealed a similar behavior to the bare counterpart (Figure S8, Supporting Information), which agrees with the cracking tendency discussed earlier.

3. Conclusions

In this study, conformal nanoscale coatings of LiHEO and HEO were successfully applied to a Ni-rich NCM cathode material, NCM851005, using photonic curing. The surface coatings significantly improved the cycling stability. In particular, they effectively mitigated structural changes caused by the reaction between cathode material and electrolyte. Compared to uncoated NCM851005, secondary particle cracking was significantly reduced after coating, thereby preventing electrolyte penetration into the bulk of the NCM851005 and further side reactions at the free surface of the primary grains. This results in more stable cycling even at high cutoff potentials. In addition, by comparing the cycling performance of the HEO- and LiHEO-coated NCM851005, we found that the ionic and electronic partial

conductivities of the coating play an important role in improving stability. Thus, this work shows that mixed ionic–electronic conductors may serve as advanced coating materials for next-generation battery electrodes. Nevertheless, more work is needed for an in-depth understanding of the mechanisms that are responsible for the enhanced performance of the LiHEO-coated NCM851005 after annealing in air, as opposed to oxygen, i.e., determining the influence of residual lithium compounds on the surface and cation interdiffusion.

The successful implementation of the photonic coating technology provides an opportunity to test new materials and to tailor coating morphology and composition. Additionally, the effective application of HEO-based coatings to a Ni-rich NCM demonstrates the potential of the technology in high-voltage cathode systems. HEOs have proven to be promising conversion anodes,[25,26] and in this study, they served as advanced coatings to improve the cycling performance of a high-capacity cathode material. In the future, other types of conversion materials with mixed ionic–electronic conductivity should be explored to exploit the beneficial properties and synergies offered by high-entropy materials.

4. Experimental Section

LiHEO-Coated NCM851005: For the preparation of 20 mg $Li_{0.33}(MgCoNiCuZn)_{0.67}O$ (LiHEO), 8.34 mg $LiNO_3$, 12.59 mg $Mg(NO_3)_2 \cdot 6H_2O$, 14.29 mg $Co(NO_3)_2 \cdot 6H_2O$, 14.28 mg $Ni(NO_3)_2 \cdot 6H_2O$, 11.42 mg $Cu(NO_3)_2 \cdot 2.5H_2O$, and 14.61 mg $Zn(NO_3)_2 \cdot 6H_2O$ were dissolved in 48 mL ethanol. Then, 1 g NCM851005 (BASF SE) was added under constant stirring at ambient temperature (for 1 h), followed by heating at 60 °C to induce solution evaporation. The powder material obtained was evenly dispersed on a silicon wafer and subjected to photonic curing (Sinteron 2000, Xenon Corp) at 3 kV for 75 s. Irradiation was repeated six times with shaking and cooling steps in between. The powder calcined in air at 600 °C was denoted as LiHEO@NCM005, while that calcined under flowing oxygen at 600 °C is referred to as LiHEO@NCM851005-Oxygen.

HEO-Coated NCM851005: For the preparation of 20 mg (MgCoNiCuZn)O (HEO), 14.62 mg $Mg(NO_3)_2 \cdot 6H_2O$, 16.59 mg $Co(NO_3)_2 \cdot 6H_2O$, 16.58 mg $Ni(NO_3)_2 \cdot 6H_2O$, 13.26 mg $Cu(NO_3)_2 \cdot 2.5H_2O$, and 16.96 mg $Zn(NO_3)_2 \cdot 6H_2O$ were dissolved in 0.48 mL ethanol. The other steps in the synthesis were identical to the LiHEO@NCM851005 described earlier. The power calcined in air at 600 °C is denoted as HEO@NCM851005, while that calcined under oxygen at 600 °C is referred to as HEO@NCM851005-Oxygen.

XRD: XRD patterns of all pristine powders were measured using an STOE StadiP diffractometer in transmission geometry at room temperature utilizing monochromatic Mo-Kα_1 radiation ($\lambda = 0.7093$ Å, $U = 50$ kV, $I = 40$ mA) and a MYTHEN 1 K strip detector (DECTRIS). The samples were flame-sealed in borosilicate capillaries (0.48 mm inner diameter, 0.01 mm wall thickness; Hilgenberg).

SEM: The microstructure of the pristine and cycled electrodes was examined using an SEM (Leo 1530) operated at 5 kV acceleration voltage and with 4 mm as working distance. Sample cross sections were prepared using a dual-beam FIB in an FEI Strata 400S at 30 kV. During sample preparation and processing, carbon layers were deposited by ion-beam-induced deposition to protect the surface coating. Samples were dispersed on carbon tape in an Ar-filled glove box and transferred to the SEM/FIB chamber within 30 s to avoid extended air exposure.

Transmission Electron Microscopy: High-resolution transmission electron microscopy (TEM), CBED, and EDX spectroscopy data were collected using a double-corrected Themis-Z microscope (Thermo Fisher Scientific) at an accelerating voltage of 300 kV, equipped with HAADF–STEM and Super-X EDX detectors. The CBED patterns were collected

using a Gatan OneView IS camera with a screen current of $\approx$10 pA, a small convergence semi-angle of 0.47 mrad, and a camera length of 580 mm. The beam current used to acquire the STEM–EDS was 200 pA. The TEM samples were prepared by FIB techniques using an FEI Strata 400S. A carbon layer was first coated onto the surface of the particles as a protective coating. They were milled at 30 kV and finally polished at 2 kV.

Raman Spectroscopy: Raman spectra were collected in the wavenumber region of 100–1000 cm^{-1} using an inVia confocal Raman microscope (RENISHAW). It should be noted that the infrared laser ($\lambda = 785$ nm, maximum laser power of 300 mW) and the green laser ($\lambda = 532$ nm, maximum laser power of 50 mW) could not be used for these samples due to resonance effects. This could be due to the presence of luminescent lanthanide ions. Therefore, a He–Ne laser ($\lambda = 633$ nm, 50 mW) was used for reliable results. A grating with groove density of 1800 groves mm^{-1} (1200 lines mm^{-1}) and a 50$\times$ objective lens were used to collect the Raman spectra. Depth profiling of the samples was not possible as the signal-to-noise ratio declined significantly. To avoid laser-irradiation-induced structural phase transition, an accumulation time of 2 s and a laser power of $\approx$1 mW ($<$10%) were used, while every spectrum recorded resulted from an average of four acquisitions. The samples for the Raman measurements were flame-sealed in borosilicate capillaries (0.48 mm inner diameter, 0.01 mm wall thickness; Hilgenberg).

Electrochemical Characterization: Electrode tapes were prepared by thoroughly mixing 90 wt% cathode material, 5 wt% Super C65 carbon black, and 5 wt% polyvinylidene fluoride (Solef 5130, Solvay) with N-methyly-2-pyrrolidone as the solvent. The slurry was tape cast using a doctor blade (200 μm slit thickness) onto Al foil and left for drying overnight. All tapes were prepared in an Ar-filled glove box to avoid contamination. The electrodes were cut using a precision cutter to 13 mm diameter circular discs. Half-cells were assembled by using standard liquid electrolyte composed of 1 M LiPF$_6$ in 3:7 by weight of ethylene carbonate and ethyl methyl carbonate. Glass fiber (GF/C, Whatman) was used as the separator. The cycling performance was tested in a climate chamber at room temperature. And, 1 C is defined as 200 mA g^{-1}. The areal loading was maintained in a range of 1–2 mg cm^{-2}.

Supporting Information

Supporting Information is available from the Wiley Online Library or from the author.

Conflict of Interest

The authors declare no conflict of interest.

Data Availability Statement

The data that support the findings of this study are available from the corresponding author upon reasonable request.

[1] J. B. Goodenough, K.-S. Park, *J. Am. Chem. Soc.* **2013**, *135*, 1167.
[2] M. Armand, *Nat. Lithium Battery Nat.* **2001**, *414*, 359.
[3] M. Fichtner, K. Edström, E. Ayerbe, M. Berecibar, A. Bhowmik, I. E. Castelli, S. Clark, R. Dominko, M. Erakca, A. A. Franco, A. Grimaud, B. Horstmann, A. Latz, H. Lorrmann, M. Meeus, R. Narayan, F. Pammer, J. Ruhland, H. Stein, T. Vegge, M. Weil, *Adv. Energy Mater.* **2021**, *12*, 2102904.
[4] H. Lv, C. Li, Z. Zhao, B. Wu, D. Mu, *J. Energy Chem.* **2021**, *60*, 435.
[5] Z. Ye, L. Qiu, W. Yang, Z. Wu, Y. Liu, G. Wang, Y. Song, B. Zhong, X. Guo, *Chem. A: Eur. J.* **2021**, *27*, 4249.
[6] S. T. Myung, F. Maglia, K. J. Park, C. S. Yoon, P. Lamp, S. J. Kim, Y. K. Sun, *ACS Energy Lett.* **2017**, *2*, 196.
[7] W. Li, E. M. Erickson, A. Manthiram, *Nat. Energy* **2020**, *5*, 26.
[8] S. S. Zhang, *Energy Storage Mater.* **2020**, *24*, 247.
[9] L. de Biasi, B. Schwarz, T. Brezesinski, P. Hartmann, J. Janek, H. Ehrenberg, Structural Chemical, *Adv. Mater.* **2019**, *31*, 1900985.
[10] L. Song, J. Du, Z. Xiao, P. Jiang, Z. Cao, H. Zhu, *Front. Chem.* **2020**, *8*.
[11] Y. Su, G. Chen, L. Chen, Q. Li, Y. Lu, L. Bao, N. Li, S. Chen, F. Wu, *Chin. J. Chem.* **2020**, *38*, 1817.
[12] W. Liu, X. Li, D. Xiong, Y. Hao, J. Li, H. Kou, B. Yan, D. Li, S. Lu, A. Koo, K. Adair, X. Sun, *Nano Energy* **2018**, *44*, 111.
[13] A. Martens, C. Bolli, A. Hoffmann, C. Erk, T. Ludwig, M. El Kazzi, U. Breddemann, P. Novák, I. Krossing, *J. Electrochem. Soc.* **2020**, *167*, 070510.
[14] F. Schipper, H. Bouzaglo, M. Dixit, E. M. Erickson, T. Weigel, M. Talianker, J. Grinblat, L. Burstein, M. Schmidt, J. Lampert, C. Erk, B. Markovsky, D. T. Major, D. Aurbach, *Adv. Energy Mater.* **2018**, *8*, 1701682.
[15] S. W. Lee, M. S. Kim, J. H. Jeong, D. H. Kim, K. Y. Chung, K. C. Roh, K. B. Kim, *J. Power Sources* **2017**, *360*, 206.
[16] P. Yan, J. Zheng, J. Liu, B. Wang, X. Cheng, Y. Zhang, X. Sun, C. Wang, J. G. Zhang, *Nat. Energy* **2018**, *3*, 600.
[17] I. D. Scott, Y. S. Jung, A. S. Cavanagh, Y. Yan, A. C. Dillon, S. M. George, S. H. Lee, *Nano Lett.* **2011**, *11*, 414.
[18] D. Bérardan, S. Franger, A. K. Meena, N. Dragoe, *J. Mater. Chem. A* **2016**, *4*, 9536.
[19] M. Moździerz, J. Dąbrowa, A. Stępień, M. Zajusz, M. Stygar, W. Zając, M. Danielewski, K. Świerczek, *Acta Mater.* **2021**, *208*, 116735.
[20] L. Wang, J. Qin, Z. Bai, H. Qian, Y. Cao, H. M. K. Sari, Y. Xi, H. Shan, S. Wang, J. Zuo, X. Pu, W. Li, J. Wang, X. Li, *Small Struct.* **2022**, *2100233*, 2100233.
[21] J. Sicklinger, M. Metzger, H. Beyer, D. Pritzl, H. A. Gasteiger, *J. Electrochem. Soc.* **2019**, *166*, A2322.
[22] F. Walther, F. Strauss, X. Wu, B. Mogwitz, J. Hertle, J. Sann, M. Rohnke, T. Brezesinski, J. Janek, *Chem. Mater.* **2021**, *33*, 2110.

**ADVANCED
SCIENCE NEWS**

www.advancedsciencenews.com

**small
structures**

www.small-structures.com

[23] F. Reissig, M. A. Lange, L. Haneke, T. Placke, W. G. Zeier, M. Winter, R. Schmuch, A. Gomez-Martin, *ChemSusChem* **2022**, *15*, e202200078.

[24] S. Schweidler, L. de Biasi, G. Garcia, A. Mazilkin, P. Hartmann, T. Brezesinski, J. Janek, *ACS Appl. Energy Mater.* **2019**, *2*, 7375.

[25] A. Sarkar, L. Velasco, D. Wang, Q. Wang, G. Talasila, L. de Biasi, C. Kübel, T. Brezesinski, S. S. Bhattacharya, H. Hahn, B. Breitung, *Nat. Commun.* **2018**, *9*, 3400.

[26] N. Qiu, H. Chen, Z. Yang, S. Sun, Y. Wang, Y. Cui, *J. Alloys Compd.* **2019**, *777*, 767.